



**HAL**  
open science

## Volumetric measurements by tomographic PIV of grid generated turbulence in an open channel flow

Thomas Earl, Lionel Thomas, Steve Cochard, Riadh Ben-Salah, Benoit Tremblais, Laurent David

► **To cite this version:**

Thomas Earl, Lionel Thomas, Steve Cochard, Riadh Ben-Salah, Benoit Tremblais, et al.. Volumetric measurements by tomographic PIV of grid generated turbulence in an open channel flow. Eighth International Symposium on Turbulence and Shear Flow Phenomena (TSFP8), Aug 2013, Poitiers, France. hal-00913316

**HAL Id: hal-00913316**

**<https://hal.science/hal-00913316>**

Submitted on 3 Dec 2013

**HAL** is a multi-disciplinary open access archive for the deposit and dissemination of scientific research documents, whether they are published or not. The documents may come from teaching and research institutions in France or abroad, or from public or private research centers.

L'archive ouverte pluridisciplinaire **HAL**, est destinée au dépôt et à la diffusion de documents scientifiques de niveau recherche, publiés ou non, émanant des établissements d'enseignement et de recherche français ou étrangers, des laboratoires publics ou privés.

# VOLUMETRIC MEASUREMENTS BY TOMOGRAPHIC PIV OF GRID GENERATED TURBULENCE IN AN OPEN CHANNEL FLOW

## Thomas A Earl

School of Civil Engineering  
The University of Sydney  
Rm 478 Bldg J05, Shepherd St,  
The University of Sydney 2006, AUS.  
thomas.earl@sydney.edu.au

## Lionel Thomas

Institut P', UPR3346  
Université de Poitiers - ENSMA  
Boulevard Marie et Pierre Curie BP 30179,  
F86962 Futuroscope Chasseneuil, FR.  
lionel.thomas@univ-poitiers.fr

## Steve Cochard

School of Civil Engineering  
The University of Sydney  
Rm 341 Bldg J05, Shepherd St,  
The University of Sydney 2006, AUS.  
steve.cochard@sydney.edu.au

## Riadh Ben Salah

Institut XLIM-SIC, UPR3346  
Université de Poitiers  
Boulevard Marie et Pierre Curie, BP 30179,  
F86961 Futuroscope Chasseneuil, FR.  
riadh.ben-salah@univ-poitiers.fr

## Benoît Tremblais

Institut XLIM-SIC, UPR3346  
Université de Poitiers  
Boulevard Marie et Pierre Curie, BP 30179,  
F86962 Futuroscope Chasseneuil, FR.  
benoit.tremblais@univ-poitiers.fr

## Laurent David

Institut P', UPR3346  
Université de Poitiers  
Boulevard Marie et Pierre Curie BP 30179,  
F86962 Futuroscope Chasseneuil Cedex, FR.  
laurent.david@univ-poitiers.fr

## ABSTRACT

This paper investigates the energy dissipation rate behind two combinations of trash racks (or meshes) in an open channel flow. Five trash rack assemblies divided the flume into four identical pools in the downstream direction. The global characteristics of the flow were compared with Tomo-PIV measurements that were taken in the water column of the flow. From the Tomo-PIV measurements, the instantaneous structures in the flow were visualised and the decay of turbulent kinetic energy and energy dissipation analysed.

## INTRODUCTION

A survey of the literature reveals that there is no shortage of experimental data that has challenged the locally homogenous assumption and show evidence the equilibrium similarity proposal. Comte-bellott & Corrsin (1966) was perhaps the first to report experimental values where the decay coefficient differed from that originally presented Batchelor & Taylor (1947).

Lavoie *et al.* (2007), using different sized regular grids in a wind tunnel to invoke reported divergence from the expected decay, even after employing a contraction in his wind tunnel flow to increase the isotropy. The study of turbulence generated by fractal grids (Gomes-Fernandes *et al.* (2012), Valente & Vassilicos (2011), Mazellier & Vassilicos (2010)) i.e. turbulence with different input generation has also pointed to non-Kolmogorov type energy dissipation.

The experimental techniques used to measure turbulence have switched from invasive techniques, such as hot wires to, in the last two decades, optical methods such as PIV. Optical techniques have the advantages of being essentially non-invasive (assuming the addition of particles does not change the flow characteristics) and that multiple components of velocity of the flow can be extracted over a spatial range simultaneously, along with the spatial gradients directly. See Adrian (1991), Westerweel *et al.* (1997) and Fayolle *et al.* (1998) for examples of early PIV studies.

There are a number of disadvantages of the PIV methods, namely that the correlation windows act as a low pass spatial filter (Foucaut *et al.*, 2004). Conversely, if the resolution of the PIV system can resolve scales smaller than the Kolmogorov scales, the velocity fluctuations can superficially increase the measured dissipation rate and needs to be corrected (Tanaka & Eaton, 2007).

Cardesa *et al.* (2012) summarise some salient PIV studies of grid generated turbulence. Similar to this study, Cardesa *et al.* (2012) have investigated turbulence in an open channel flow, albeit using 2D PIV in the near the channel inlet location. In the present study, we will use a fully three dimensional technique to measure the flow, namely tomo-PIV (Elsinga *et al.*, 2006). A recent stereo PIV and tomo-PIV study of grid generated turbulence by Buchmann *et al.* (2010) investigated and compared the performance of the two methods and it was shown that the tomo-PIV technique could retrieve the main turbulence and dissipation characteristics. Worth *et al.* (2010) have investigated

the resolution effects of Tomo-PIV measurements of turbulence and compares the results to DNS data of homogeneous isotropic turbulence.

In this study, an inclined open channel flow where, in order to prevent the flow accelerating down the slope, a series of trash racks, or regular grids, is used to convert potential energy into turbulent kinetic energy that is dissipated along the channel is investigated. The global power and dissipation characteristics of the flow across each pool were determined, explained further herein. Tomographic PIV measurements were taken to see the local energy dissipation behaviour and compare the global findings between the two configurations.

## EXPERIMENTAL DETAILS

Experiments were conducted in an open channel (Figure 1) at Institut Pprime at the Université de Poitiers, France. The inclined channel was rectangular in cross section with dimensions  $500 \times 304$  mm (height,  $H \times$  width,  $W$ ) and had 30 mm thick perspex walls and base to allow full optical access. The channel was divided into 4 identical pools that were separated by trash rack assemblies. The water was pumped from the lower reservoir into the upper reservoir, and the resulting flow propagated down the channel by gravity. The declination of the channel for both cases was 5%, or  $\approx 2.9^\circ$ . The weir gate height was adjusted so that there was a regular head loss,  $\Delta H$ , across each trash rack with a constant flow rate of  $Q = 34$  L/s for both trash rack configurations.

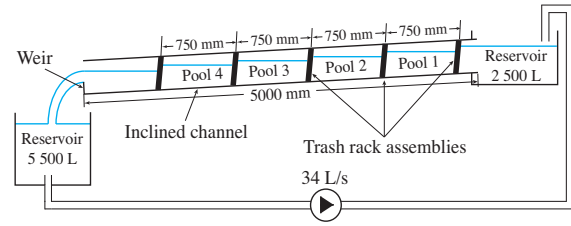


Figure 1. Schematic of the channel flow with free surface, divided into 4 identical pools by a series of regular grids

Each pool was separated by a vertical trash rack assembly. The trash racks were comprised of, from upstream to downstream, a fine wire mesh and a pair of regular grids that were fabricated from 2 mm thick stainless steel plates. The fine wire mesh ensured that any large eddies from the previous pool were broken up before entering the next pool. The grid pairs used were G1-G2 and G3-G4, with square opening geometries as shown in Figure 2. Stream-wise spacing between the components of the trash rack was 90 mm. The solidity ratios  $\sigma$ , defined by  $\sigma = (D/M)(2 - D/M)$ , are given in Figure 2, where  $D$  is the width of each bar and  $M$  is the centre-to-centre bar spacing of the grid. The characteristics of the G2 and G4 grids are used for the dimensionless analysis, as the resulting turbulence downstream is characterised by these grids.

The bulk mean velocity of the flow through each pool,  $\bar{U} = Q/(h_c W)$ , where  $h_c$  is the flow depth at the centre of the pool, was approximately 0.35 m/s and 0.32 m/s for the G1-G2 and G3-G4 configurations respectively. Likewise, the respective Reynolds numbers,  $Re$ , with respect to grid geometry were 4300 and 9600 which are in the higher

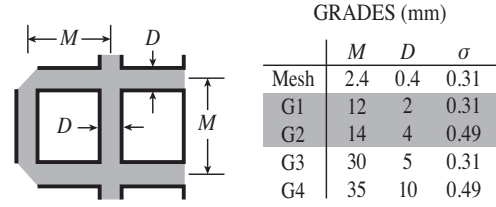


Figure 2. The geometry of the regular, square opening grids fashioned onto a thin metal plate, with dimensions and solidity ratio,  $\sigma$

ranges of recent PIV studies (Cardesa *et al.* (2012)). The hydraulic diameter,  $D_H = h_c W / (2h_c + W)$  for this channel was in the order of 0.1 m for both grid combinations. Both flows were subcritical, each with a Froude Number  $Fr = \bar{U} / \sqrt{g h_c} \approx 0.2$ .

Despite a subcritical  $Fr$ , the head loss through the grids induced a localised critical flow on the free surface, where the flow was observed to jet out from behind the trash rack and form a standing wave on the surface. This turbulent mixing had the consequence of entraining bubbles into the flow.

## BULK FLOW PROPERTIES

The flow down the channel is globally stationary, and therefore the energy losses are the same for each pool. By applying Bernoulli's (Eq 1) between the centre points of two successive pools, it is possible to approximate the bulk head loss  $\Delta H_B$ , which is a combination of the head loss through the grids  $\Delta H$ , the skin friction along the channel boundaries and the dissipation of the turbulent kinetic energy, so that

$$\frac{p_1}{\rho g} + \frac{U_1^2}{2g} + z_1 = \frac{p_2}{\rho g} + \frac{U_2^2}{2g} + z_2 + \Delta H_B \quad (1)$$

where the pressure  $p$ , water density  $\rho$  and velocity  $U$  are the same in successive pools. Therefore,  $\Delta H$  is balance only by the change in elevation  $z_1 - z_2$  that accelerates the flow. The volumetric dissipated power  $P_V$  in a pool, per unit volume can be found by computing the ratio of the work done to the water volume:

$$P_V = \frac{\rho g Q \Delta H_B}{L W h_c} = \bar{\epsilon} \rho \quad (2)$$

where  $L$  is the distance between sequential trash racks. The bulk dissipated energy  $\bar{\epsilon}$  can then be determined from the same equation. Table 1 summarises the salient results of this analysis, where it can be seen that there is a greater  $\Delta H$  in the G1-G2 case and a lower  $h_c$ , contributing to a higher  $\bar{\epsilon}$  than for G3-G4. The Kolmogorov scale  $\eta_B = (v^3/\bar{\epsilon})^{1/4}$  is introduced in Table 1 to indicate the dissipative scales of the flow.

## TOMOGRAPHIC PIV DETAILS

Tomo-PIV measurements were taken in pool 3 to ensure a fully developed flow (Figure 3). The tomo-PIV sys-

Table 1. Salient properties of the flow for each grid combination

Case	G1–G2	G3–G4
$h_c$	320 mm	355 mm
$\Delta H$	60 mm	40 mm
$P_V$	$171 \text{ kg m}^{-1} \text{ s}^{-3}$	$154 \text{ kg m}^{-1} \text{ s}^{-3}$
$\bar{\epsilon}$	$0.171 \text{ m}^2 \text{ s}^{-3}$	$0.155 \text{ m}^2 \text{ s}^{-3}$
$\eta_B$	0.067 mm	0.068 mm

tem was comprised of four 1600 × 1200 px 8 bit cameras positioned symmetrically in an inverted pyramid configuration, with declination and inward angles of approximately 20° (see Figure 3). The camera orientation was a balance between approaching the optimum camera subtended angles for tomo-PIV (shown to be 30° for synthetic images Thomas *et al.* (2013)) and reducing the aberrations of the particle images due to the high refractive index change at the interface of the air and the channel. Although water prisms can be used to negate the optical aberrations by ensuring the air-perspex interface is perpendicular to the camera lens axes, this is not always convenient, particularly when different measurement locations are intended for analysis and was not used in this study.

All cameras were fitted with 50 mm lenses, 532 nm pass optical filters (corresponding to the laser wavelength) and lens mounted Scheimpflug adapters, adjusted so that the camera focal planes were coincident with the laser sheet. Additionally, the apertures were set at  $f_{\#} = 22$  during acquisition for superior depth of field. Neutrally buoyant, spherical, polyamide particles of mean diameter  $d_{50} \approx 56 \mu\text{m}$  and density  $1.02 \text{ g/cm}^3$  were used to seed the flow. The particle density, size and quantity were carefully selected to achieve a compromise between signal to noise ratio, resolution, particle image size, particularly in the study of turbulence calculations, to ensure that the particles follow the flow truthfully.

A 15 mm thick laser sheet was used to illuminate the measurement volume, realised with a double head YAG laser with 120 mJ per pulse. The measurement volume in the centre of the pool was  $100 \times 70 \times 15 \text{ mm}^3$  ( $X \times Y \times Z$ ) and aligned with the flow direction in pool 3. The time between corresponding images,  $\Delta t$ , was 2 ms, chosen to achieve mean particle displacements of  $\sim 8$  px for each camera. These double-quadruplicate images (8 of which make a velocity field) were acquired at 5 Hz. The tomographic reconstructions and correlations were made using the SLIP library (Tremblais *et al.*, 2010) developed at the Université de Poitiers. Reconstruction was performed with MinLOS–MART (minimum line-of-sight, multiplicative algebraic reconstruction technique) (Thomas *et al.*, 2013).

### Treatment of data

The tomo-PIV process is sensitive to a number of parameters, so image processing, calibration methods, treatment of the reconstructed volume and post processing of the velocity fields were carefully considered (see for example Scarano (2013)). A pinhole model was used to calibrate the cameras, improved with a volumetric self calibra-

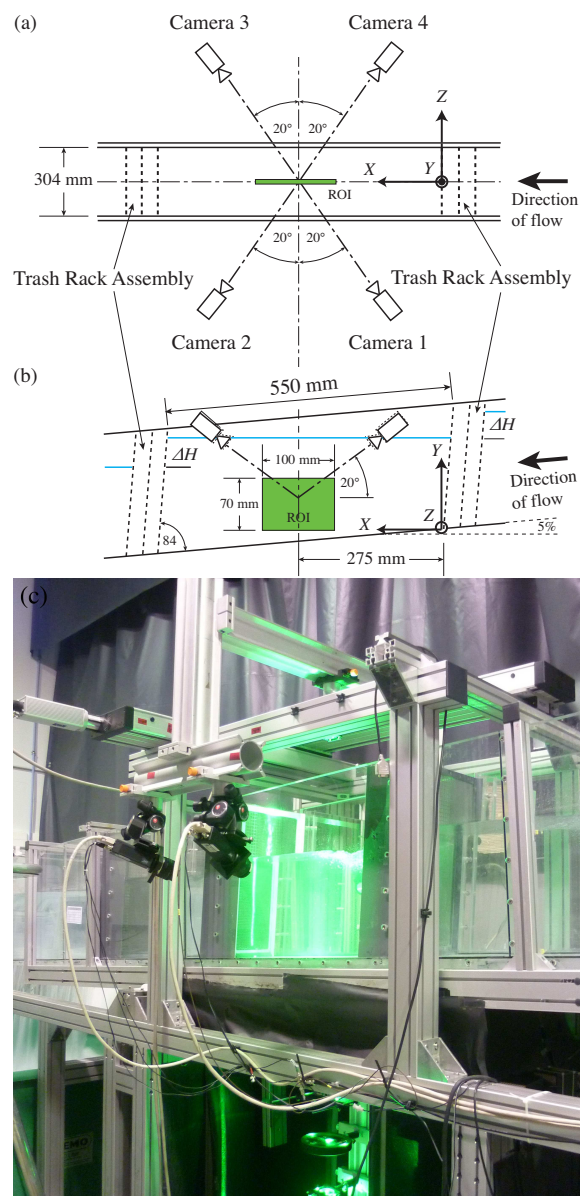


Figure 3. Schematic of Pool 3 showing measurement volume or region of interest (ROI) in (a) top view and (b) side view. The origin and axis orientation along with inverted pyramid configuration of the cameras are shown. A photograph is shown in (c), highlighting the position of the cameras and laser optics.

tion technique analogous to Wieneke (2008). Image processing to remove background noise was conducted with a sliding  $32 \times 32$  px mean window. The processed images to be reconstructed had a homogeneous particle per pixel of  $ppp \approx 0.02$ , or an image source density  $N_s \approx 0.4$ , for all cameras at both time-steps. The resulting images were a compromise between obtaining maximum possible resolution, reducing the number of ghost particles and elevating the signal to noise ratio to be as high as possible. A gaussian filtering kernel was then applied to smooth particle images, the kernel size chosen to match the average particle diameter.

Small bubble entrainment in the water due to the free surface and subsequent turbulent mixing through the trash rack assembly was evident and detracted from the quality of the reconstruction. The bubbles had two main effects: pri-

marily, they created image ‘particles’ larger than the mean when in the illuminated volume that were at times large enough to cause over exposure and an Airy disk effect on the images. The second problem, which was more specific to the G3-G4 case was that the bubbles in the foreground, that is, between the illuminated volume and the camera (i.e. not illuminated directly by the laser sheet) perturbed the line-of-sight of the particles and left regions in the images where there appeared to be no particles. No standard image treatment was able to rectify these effects, therefore these images were disregarded.

A  $64 \times 64 \times 64$  voxel correlation volume with 50% overlap was used to find the most probable displacement of particles across the two reconstructed volumes. This resulted in 3360 vectors per acquisition at a spatial resolution,  $\Delta x$  in each direction of 3 mm. A  $5 \times 5 \times 5$  filter kernel was used that replaced spurious vectors with the median vector in the filtering kernel. As tomographic reconstruction had been shown to be particularly susceptible to noise Worth *et al.* (2010), a bilateral filter was used to filter the velocity fields, which was preferred over a gaussian filter as it preserves edges. The quality of the tomographic PIV results was quantified by assessing the calculated divergence of the velocity field, and the probability distribution functions of the velocity displacements.

## RESULTS

This section describes the results obtained from the Tomo-PIV measurements.

### Mean Velocity Fields

Figure 4 shows contours of the magnitude of velocity  $U = \sqrt{u^2 + v^2 + w^2}$  averaged over each  $Z$  plane and for each velocity field. Similarly, the velocity vectors are shown with the averaged planar components  $u$  and  $v$  to highlight the direction of the flow.

Figure 4, shows two configurations generate different flow regimes. In the G1-G2 case, there is a jetting of the flow under the measured region. This is contrary to the G3-G4 case, which is slower and tends to lose velocity closer to the bottom of the channel. For both cases, the range of velocity does not exceed 10%.

### Instantaneous Velocity Fields

From the fully volumetric velocity field, the instantaneous vorticity fields  $\omega$  were calculated to observe and compare the vorticity structures present in each configuration. The tomo-PIV process allows for full recovery of the velocity gradient tensors and hence vorticity directly, without the need for assuming stationary turbulence.

In Figure 5, the vorticity isosurfaces showing  $\omega_z$  are plotted. The presence and power of vortex structures is greater, as expected, in the G3-G4 case compared to the G1-G2 case. It is noted that G3-G4 has larger grid sizes in the trash rack and, in a dimensionless sense, it is nearer to the back of the trash rack. In the following section it is shown that these results give good qualitative agreement to the decay of vorticity in the streamwise direction system (Figure 7b).

### Resolution

The field of view size and resolution is a compromise between capturing global flow features, such as structures,

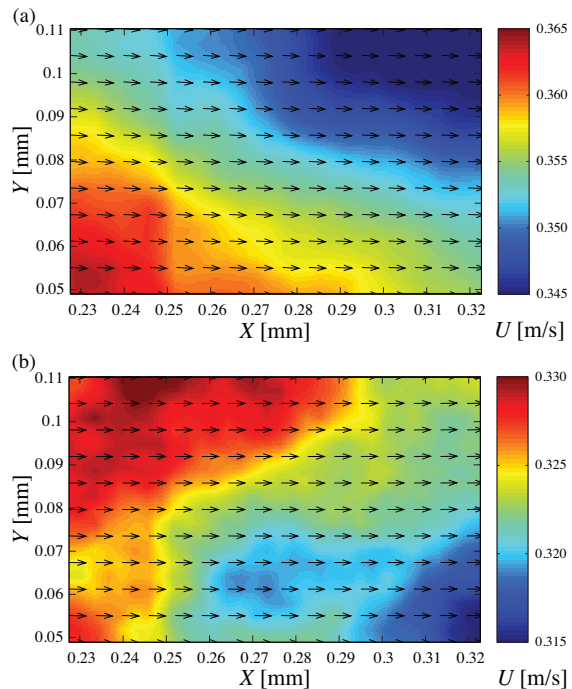


Figure 4. Contours plots of the magnitude of velocity overlaid with vectors with planar  $u$  and  $v$  components for (a) G1-G2 and (b) G3-G4. (one quarter of the vectors shown)

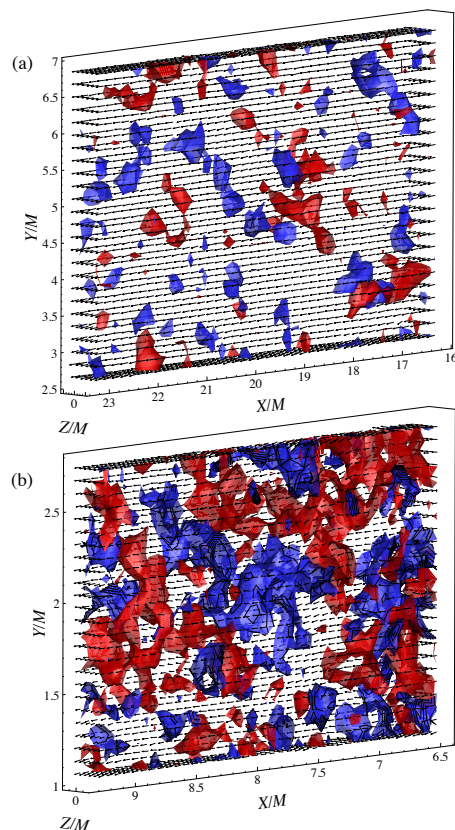


Figure 5.  $\omega_z$  iso-contours at  $0.008 \text{ m}^{-2}$  (red) and  $-0.008 \text{ m}^{-2}$  (blue) for configuration (a) G1-G2 and (b) G3-G4 with velocity vectors.

and resolution. It was known *a priori* that these PIV measurements would not capture the Kolmogorov scale resolution. To capture the Kolmogorov scale, the optimum vector spacing must be  $\eta_b/10 < \Delta x < \eta_b/2$ , where  $\eta$  is the Kolmogorov microscale (Tanaka & Eaton, 2007). But experiments have shown that as  $\Delta x$  becomes smaller, the noise also increases. Seeding density increases the effect of ghost particles (for example, Elsinga & Westerweel (2011), Novara *et al.* (2010)), which has the effect of broadening the correlation peak. In addition, it was found that the addition of more particles in the flow had the effect of detrimentally increasing the turbidity of the water, and hence signal to noise ratio.

### Turbulence Quantities

In this section the turbulence statistics of the flow is considered. The velocity gradients used to calculate the divergence  $\nabla \mathbf{u}$  are shown in Figure 6a for the G1–G2 case, the results of which show smooth gradients with mean zero, which indicates a good quality of results. The normalised turbulence intensity,  $\mathbf{u}'/\bar{u}$  as it decays in the streamwise direction are plotted in Figure 6b. From this figure it can be seen that in this region of the pool, for both cases, the contribution to the turbulent kinetic energy from the three components of velocity is seen to be equal, or isotropic.

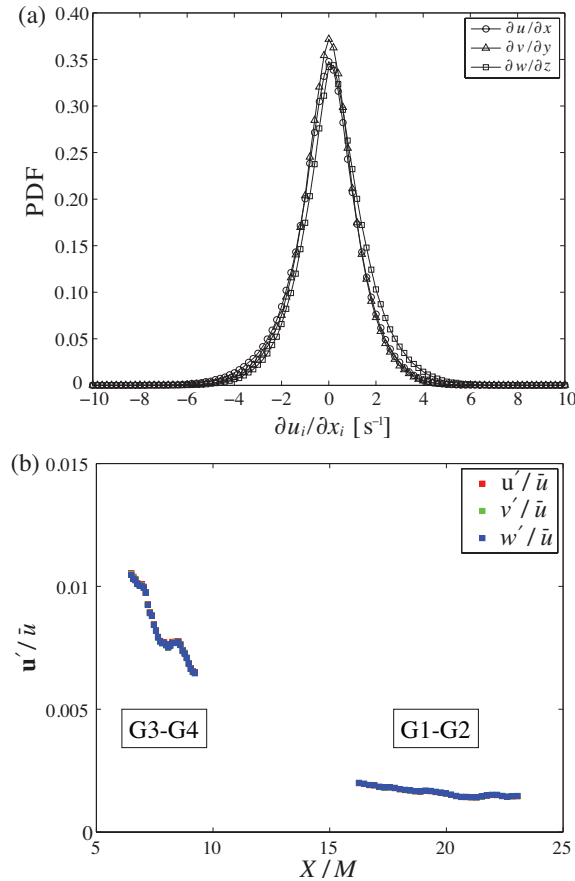


Figure 6. (a) The velocity gradient pdf for the divergence calculation, and (b) mean normalised turbulent kinetic energy along the streamwise direction for the 3 velocity components.

### Energy Dissipation

The mean energy dissipation from the tomo-PIV measurements is obtained from Equation 3. It is used to calculate the mean local dissipation rate  $\langle \varepsilon \rangle$  in the flow, where the angled brackets indicate ensemble averaging. It was verified that it does not evolve over time, and convergence is achieved after 200 velocity fields (not shown for brevity).

$$\langle \varepsilon \rangle = \nu \left\{ 2 \left( \left\langle \left( \frac{\partial u}{\partial y} \frac{\partial v}{\partial x} \right) \right\rangle + \left\langle \left( \frac{\partial u}{\partial z} \frac{\partial w}{\partial x} \right) \right\rangle + \left\langle \left( \frac{\partial v}{\partial z} \frac{\partial w}{\partial y} \right) \right\rangle \right) + \left\langle \left( \frac{\partial u}{\partial y} \right)^2 \right\rangle + \left\langle \left( \frac{\partial v}{\partial x} \right)^2 \right\rangle + \left\langle \left( \frac{\partial u}{\partial z} \right)^2 \right\rangle + \left\langle \left( \frac{\partial w}{\partial x} \right)^2 \right\rangle + \left\langle \left( \frac{\partial v}{\partial z} \right)^2 \right\rangle + \left\langle \left( \frac{\partial w}{\partial y} \right)^2 \right\rangle \right\} \quad (3)$$

In Figure 7a, the energy dissipation  $\langle \varepsilon \rangle$ , normalised by the viscosity, is averaged over time and for the position downstream. Figure 7b shows the components of the vorticity squared, also along the streamwise direction. These figures show an exponential decay of energy in the flow.

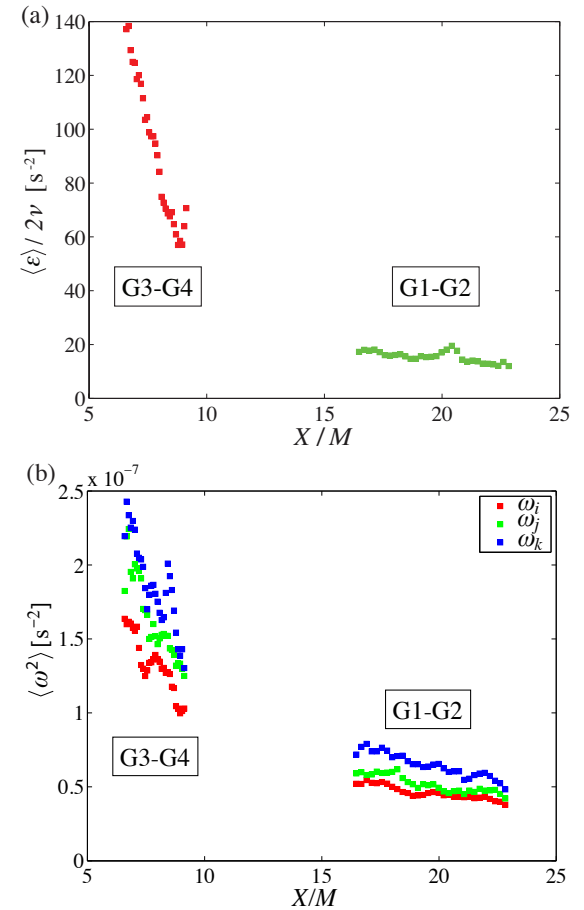


Figure 7. (a) energy dissipation averaged along each stream-wise position (b) decay of the vorticity along the streamwise direction

In Figure 7b, anisotropy can be observed. The vorticity in Figure 7b has a stronger  $\omega_k$  component than the  $\omega_i$  and  $\omega_j$  components, corresponding to vortices that ‘roll’ down the flow, which seems reasonable because of the action of the free surface tumbling after the grids. It can also be noted that the vorticity plot is inherently more noisy due to the differences of velocity gradients being squared. One must also note however that there is likely to be tomographic reconstruction effects that contribute to this anisotropy result too, such as elongated particle reconstruction in the out-of-plane direction Elsinga *et al.* (2006). This remains to be confirmed.

The analysis of  $\langle \varepsilon \rangle$  from the tomographic PIV is compared to  $\bar{\varepsilon}$ . It can be seen that the energy dissipation due to the decay of turbulent kinetic energy is higher in G3–G4 than for G1–G2 (Figure 7), the inverse of the result found for  $\bar{\varepsilon}$ . This is due to the larger grid geometry creating larger structures in the flow (Figure 5). The ratio between the two calculations is defined by  $\varepsilon^* = \langle \varepsilon \rangle / \bar{\varepsilon}$ . It was found that for G1–G2 and G3–G4,  $\varepsilon^*$  was respectively in the order of 0.005 and 0.033. This range is reasonable, as the dissipation for the Tomo-PIV results are calculated only in the water column compared to  $\bar{\varepsilon}$  that encompasses all losses in the pool. In addition, the resolution of the system was not fine enough to resolve the smallest Kolmogorov scales, which is akin to applying a low pass filter on the energy spectrum.

## CONCLUSION

Tomo-PIV was used to measure the flow in a pool of an inclined open channel behind a trash rack for the first time. Two trash rack assembly configurations of different sized grids with equivalent solidity ratios were compared. Analysis of the bulk energy dissipation through the pools were compared with the energy dissipation measured directly from the three dimensional velocity field data. Analysis of the vorticity and energy dissipation show qualitative and quantitative agreement of the decay of turbulent kinetic energy following a power law. The components of vorticity show anisotropy of the decay, found by the recovery of the full velocity gradient tensors through tomo-PIV.

## ACKNOWLEDGEMENTS

The authors would like to express gratitude for the continued support of an Australian Postgraduate Award (APA) and A D McConnell scholarship. The experiments were conducted at the Université de Poitiers, France, and were funded by 13th CPER and FEDER.

## REFERENCES

Adrian, Ronald J 1991 PARTICLE-IMAGING TECHNIQUES FOR EXPERIMENTAL FLUID MECHANICS. *Annu. Rev. Fluid Mech.* **23**, 261–304.

Batchelor, G. K. & Taylor, Geoffrey 1947 Kolmogoroff’s theory of locally isotropic turbulence. *Mathematical Proceedings of the Cambridge Philosophical Society* **43** (04), 533.

Buchmann, N A, Atkinson, C & Soria, J 2010 Tomographic and Stereoscopic PIV measurements of Grid-generated Homogeneous Turbulence. In *15th Int Symp on Applications of Laser Techniques to Fluid Mechanics Lisbon, Portugal, 05-08 July, 2010*.

Cardesa, J. I., Nickels, T. B. & Dawson, J. R. 2012 2D PIV measurements in the near field of grid turbulence

using stitched fields from multiple cameras. *Experiments in Fluids* **52** (6), 1611–1627.

Comte-bellott, By Genevieve & Corrsin, Stanley 1966 The use of a contraction to improve the isotropy of grid-generated turbulence. *Journal of Fluid Mechanics* **25**, 657—682.

Elsinga, G. E., Scarano, F., Wieneke, B. & Oudheusden, B. W. 2006 Tomographic particle image velocimetry. *Experiments in Fluids* **41** (6), 933–947.

Elsinga, G E & Westerweel, J 2011 The point-spread-function and the spatial resolution of PIV cross-correlation methods. In *9TH INTERNATIONAL SYMPOSIUM ON PARTICLE IMAGE VELOCIMETRY PIV11 Tsukuba, Japan, July 21-23, 2011*.

Fayolle, J, Riou, L, David, L & Schon, J. P. 1998 The grid turbulence: Measurement of the decay rate of the turbulence intensity with image processing algorithms. In *8th International Symposium on Flow Visualisation*, pp. 125.1—125.11.

Foucaut, J M, Carlier, J & Stanislas, M 2004 PIV optimization for the study of turbulent flow using spectral analysis. *Measurement Science and Technology* **15** (6), 1046–1058.

Gomes-Fernandes, R., Ganapathisubramani, B. & Vassilicos, J. C. 2012 Particle image velocimetry study of fractal-generated turbulence. *Journal of Fluid Mechanics* **711**, 306–336.

Lavoie, P., Avallone, G., Gregorio, F., Romano, G. P. & Antonia, R. A. 2007 Spatial resolution of PIV for the measurement of turbulence. *Experiments in Fluids* **43** (1), 39–51.

Mazellier, N. & Vassilicos, J. C. 2010 Turbulence without Richardson-Kolmogorov cascade. *Physics of Fluids* **22** (7), 075101.

Novara, M., Batenburg, K. J. & Scarano, F. 2010 Motion tracking-enhanced MART for tomographic PIV. *Measurement Science and Technology* **21** (3), 1–18.

Scarano, F 2013 Tomographic PIV: principles and practice. *Meas. Sci. Technol.* **24**, 28pp.

Tanaka, Tomohiko & Eaton, John K. 2007 A correction method for measuring turbulence kinetic energy dissipation rate by PIV. *Experiments in Fluids* **42** (6), 893–902.

Thomas, L, Tremblais, B. & David, L. 2013 Optimization of the volume reconstruction for classical tomo-piv algorithms (mart, bimart and smart): synthetic and experimental studies. *Measurement Science and Technology* (SUBMITTED).

Tremblais, B, David, L, Arrivault, D, Dombre, J, Chatellier, L & Thomas, L 2010 SLIP: Simple Library for Image Processing (version 1.0), <http://www.sic.sp2mi.univ-poitiers.fr/slip/>.

Valente, P C & Vassilicos, J C 2011 The decay of turbulence generated by a class of multiscale grids. *Journal of Fluid Mechanics* **687**, 300–340.

Westerweel, J, Dabiri, D & Gharib, M 1997 The effect of a discrete window offset on the accuracy of cross-correlation analysis of digital PIV recordings. *Experiments in Fluids* **23** (September 1995), 20—28.

Wieneke, B 2008 Volume self-calibration for 3D particle image velocimetry. *Experiments in Fluids* **45**, 549–556.

Worth, N. A., Nickels, T. B. & Swaminathan, N. 2010 A tomographic PIV resolution study based on homogeneous isotropic turbulence DNS data. *Experiments in Fluids* **49** (3), 637–656.